Real-Time Observation of Nonadiabatic Bifurcation Dynamics at a Conical Intersection

Kyung Chul Woo, Do Hyung Kang, and Sang Kyu Kim*

Department of Chemistry, KAIST, Daejeon 34141, Republic of Korea

S *Supporting Information*

ABSTRACT: Looking into temporal dynamics of the reactive flux that is precisely located at the well-characterized conical intersection has been one of chemists' longstanding goals. We report here real-time nonadiabatic bifurcation dynamics in the S−CH_3 bond predissociation of thioanisole ($C_6H_5SCH_3$) in the first electronically excited state (S_1). It is found that two distinct adiabatic and nonadiabatic reaction pathways are activated simultaneously only when the vibronic state near the first conical intersection is optically accessed. Our time-resolved measurement of the product state distribution could separate two different dynamic channels unambiguously, unraveling the detailed dynamic mechanism of the nonadiabatic reaction taking place in the vicinity

of the conical intersection. The nonadiabatic channel, where the reactive flux funnels through two consecutive conical intersections along the reaction coordinate, is found to be significantly faster than the adiabatic channel along the minimum energy reaction pathway. The kinetic energy release ratio and the nonadiabatic transition probability are found to be much higher for the nonadiabatic channel than those of the adiabatic channel, giving insights into the bifurcation dynamics occurring at the conical intersection.
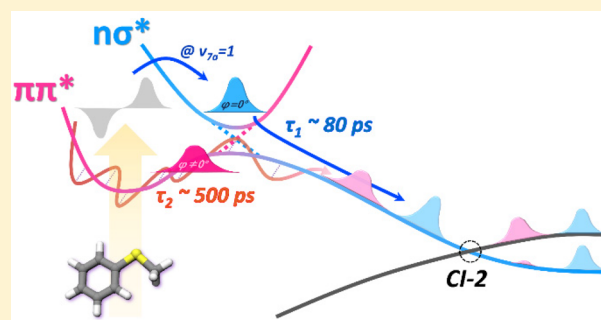
INTRODUCTION

According to Herzberg's classification, predissociation of an excited molecule takes place either by electronic (type-I) or vibrational (type-II) coupling to the reaction coordinate.[1−3] The reactive flux in the type-I case switches over to a different electronic surface by electronic coupling,[4,5] whereas it sticks to the single adiabatic potential energy surface in type-II.[6−8] In the latter, vibrational coupling to the reaction coordinate via intramolecular vibrational redistribution (IVR) and/or tunneling processes is mainly responsible for predissociation. For diatomic molecules where no curve-crossing is allowed, the type-I predissociation prevails.[9−11] For polyatomic molecules, however, differentiation of type I and II seems to be not unambiguous. This is because of the complexity of potential energy surfaces near the surface-crossing region where nonadiabatic electronic coupling is facilitated. For instance, we may consider surface-crossing of an optically bright bound state and a slightly upper-lying optically dark repulsive state. If the dark state is repulsive only along a specific reaction coordinate and bound with respect to all other internal degrees of freedom, its surface crossing with the bright bound state relevant to predissociation should be quite narrowly defined in the entire phase space. Namely, the probability of the initially prepared quantum state being coupled to the reaction coordinate via direct electronic coupling could be substantially low for polyatomic molecules since it should be frustrated to find a quantum state having the right momentum for surface-crossing as the number of internal degrees of freedom increases.

Furthermore, as conical intersections lie on a multidimensional seam for polyatomic molecules,[12−15] it is nontrivial to correlate dynamic variables with nonadiabatic transition outcomes. These are the main reasons that direct probing of the conical intersection is intrinsically difficult and thus has been quite rare.

Nevertheless, capturing the conical intersection of polyatomic molecules in either a spatial or temporal domain has long been a challenging and important goal for chemists, as figuring out conical intersections has been widely regarded as essential in understanding and controlling ubiquitous nonadiabatic processes in nature. Spectroscopic perturbations in the vicinity of conical intersections had been reported in numerous cases, confirming not only the existence of a conical intersection but its significant role in nonadiabatic dynamic behavior in terms of molecular structure and chemical reactivity.[16,17] In the time domain, femtosecond (fs) wavepacket dynamics in the vicinity of the conical intersection have been explored for many interesting chemical or biological systems ranging from a small molecule of NO_2 to a complicated bacterial rhodopsin.[18−21] Conical intersection dynamics of several polyatomic molecules have also been studied in the frequency domain, providing a nonadiabatic coupling map in the nuclear configuration space.[22−26] Despite many successful experimental studies, however, the spatial and/or temporal description of the conical intersection for polyatomic molecules has not been fully

concretized to date, whereas theoretical calculations have been much evolved in terms of both stationary and dynamic aspects of the conical intersection in multidimensional ways.[27−30]

In this regard, our recent finding of nonadiabatic dynamic resonances corresponding to direct probing of the conical intersection in the photodissociation of thioanisole ($C_6H_5SCH_3$) provided a unique platform to investigate nonadiabatic dynamics near the surface-crossing region of the polyatomic system.[31] In brief, the S−CH_3 bond dissociation of thioanisole excited on the bound $\pi\pi^*$ state (S_1) takes place via coupling to the nearby repulsive $n\sigma^*$ state (S_2) as S_1 and S_2 states cross along the S−CH_3 bond elongation, giving the first S_1/S_2 conical intersection (CI-1) at the planar geometry (Figure 1). At the later stage, the second $\pi\pi/n\sigma^*$ conical
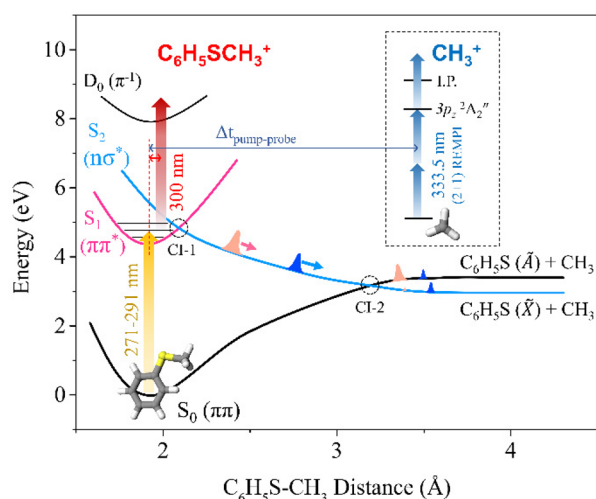

Figure 1. Schematic of the electronic potential energy surfaces of thioanisole along the S−CH_3 bond elongation coordinate. Time-resolved experimental pump−probe scheme is also visualized.

intersection (CI-2) is generated also at the planar geometry, as the repulsive S_2 state correlates to the ground $C_6H_5S\cdot$ radical ($\tilde{X}$), whereas S_0 correlates to the excited $C_6H_5S\cdot$ radical ($\tilde{A}$) diabatically. When the bond dissociation occurs adiabatically, the $\cdot CH_3 + C_6H_5S\cdot(\tilde{A})$ product channel is expected to be dominant, whereas the energetically low-lying $\cdot CH_3 + C_6H_5S\cdot$ ($\tilde{X}$) channel is produced only by nonadiabatic transition at CI-2. Experimentally, we have quantitatively measured branching ratios of nonadiabatic ($\cdot CH_3 + C_6H_5S\cdot(\tilde{X})$) versus adiabatic ($\cdot CH_3 + C_6H_5S\cdot(\tilde{A})$) channels for all well-resolved S_1 vibronic levels of thioanisole by deconvolution of the total translational distribution of fragments into the low or high kinetic energy portion, which is associated with the $C_6H_5S\cdot(\tilde{A})$ or $C_6H_5S\cdot(\tilde{X})$ channel, respectively, between which the energy gap is 3000 ± 7 cm^{-1}.[32] As expected, thioanisole riding on most of the S_1 vibronic states in the range of 0−2000 cm^{-1} above the S_1 minimum energy follows the adiabatic path, giving quite low $\tilde{X}/\tilde{A}$ product branching ratios. Surprisingly, however, the $\tilde{X}/\tilde{A}$ product branching ratio shows a dramatic increase at 722 cm^{-1} above S_1, corresponding to the 7a vibronic mode (C−S−C asymmetric stretching) excitation,[31] Figure 2. This "nonadiabatic dynamic resonance" observed only at such a mode in the given energy range should reflect the dynamic role of the conical intersection that is accessed by the corresponding optical excitation. The $\tilde{X}/\tilde{A}$ branching ratio is actually supposed to be proportional to the nonadiabatic transition probability at
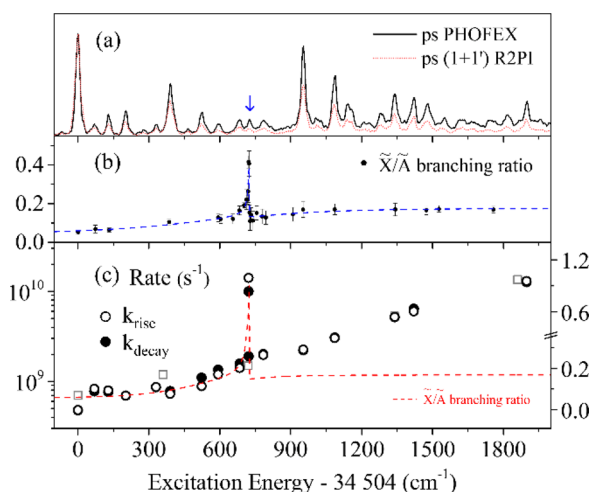

Figure 2. State-specific rate measurement. (a) Picosecond PHOFEX and (1 + 1′) R2PI spectra. At +722 cm^{-1} of internal energy, the nonadiabatic transition probability manifested by the $\tilde{X}/\tilde{A}$ branching ratio shows a sharp resonance-like feature in (b) (reprinted from ref 31). (c) Rate constants obtained from state-specific transients of $C_6H_5SCH_3^+$ (filled circles) or CH_3^+ (open circles). At +722 cm^{-1} two distinct rate constants are given from a biexponential fit to the experiment. Previously reported rate constants obtained from the femtosecond pump−probe method[37] are given as gray squares for comparison; overall rate constants are consistent with the current experiment, whereas biexponential behavior could not be observed due to the broad bandwidth of the femtosecond laser pulse. Red dotted line in (c) is the plot of the $\tilde{X}/\tilde{A}$ branching ratio, which is the same as in (b) except that the ratio is now ∼0.9 for the fast component at 722 cm^{-1} (see the text).

CI-2. Nevertheless, these two conical intersections encountered at the planar geometry along the reaction pathway are connected by the repulsive $n\sigma^*$ state, and thus quantum characteristics of the reactive flux beyond the S_1/S_2 conical intersection are not expected to be much altered at CI-2 especially with respect to vibrational modes orthogonal to the reaction coordinate. Therefore, it is most likely that the S_1/S_2 conical intersection is the fingerprint for CI-2, rationalizing the above argument that the dynamic resonance observed at the 722 cm^{-1} mode results from a sharp increase of the nonadiabatic coupling strength at the S_1/S_2 conical intersection, which leads to a resonance in the $\tilde{X}/\tilde{A}$ product branching ratio in the asymptotic region (Figure 2). In turn, the 7a vibronic mode giving the nonadiabatic dynamic resonance then provides at least a one-dimensional projection of the S_1/S_2 conical intersection in terms of its phase space, as the nonadiabaticity of the reactive flux is very sensitive to its proximity to the conical intersection in terms of energetics, structure, and nuclear momentum. Since surface crossings lie on the multidimensional seam for polyatomic molecules, it is nontrivial to characterize the conical intersection in full dimensional nuclear configuration space. In our recent works on partially deuterated thioanisoles ($C_6H_5S-CD_3$, $C_6H_5S-CH_2D$, or $C_6H_5S-CHD_2$), spectroscopic characterization of the conical intersection could be extended to the more internal degrees of freedom in the normal mode space.[14,33,34]

Our successful structural characterization of the conical intersection now provides an excellent platform to interrogate temporal behavior of the reactive flux in the vicinity of the conical intersection, which is central to a thorough understanding of nonadiabatic transitions in chemistry and biology.

Even though femtosecond wavepacket dynamic studies had been reported for a limited number of systems including thioanisole,[35−38] the reactive flux in those studies intrinsically could not be located in the narrowly defined conical intersection region. In this regard, to the best of our knowledge, temporal dynamics of the reactive flux near the well-characterized conical intersection has never been reported for polyatomic molecules to date. Herein, we report real-time nonadiabatic bifurcation dynamics of the reactive flux which is quite precisely located in the proximity of the conical intersection, giving the great opportunity to interrogate the nature of the conical intersection in terms of both structure and dynamics for the first time. In order to achieve temporal and spatial characterization of the conical intersection at the same time, the picosecond (ps) pump−probe method has been employed here. A pump laser pulse with a temporal duration of 1.5 ps and spectral width of 25 cm^{-1} could excite a specific vibronic level exclusively. Lifetimes of S_1 vibronic levels are then measured by monitoring the parent ion signal as a function of the delay time between pump and ionization (probe) laser pulses. On the other hand, appearance rates of fragments are measured by detecting the nascent ·CH_3 ($v = 0$) fragment ion signal as a function of reaction time, whereas the time-resolved velocity-map ion imaging (TR-VMI) method is used to obtain product translational distributions as a function of the reaction time.

RESULTS AND DISCUSSION

The resonant two-color two-photon ionization (R2PI) spectrum of jet-cooled thioanisole, obtained by scanning picosecond pump wavelength at a fixed probe wavelength at around zero time delay, gives rise to well-resolved S_1 vibronic quantum levels even though spectral widths associated with individual S_1–S_0 transitions are somewhat broadened compared to those in the previously reported nanosecond (ns) R2PI spectrum, Figure 2.[31] Spectral features in the photofragment excitation (PHOFEX) spectrum, which is obtained by monitoring the ·CH_3 yield at the delay time of ~2.84 ns with changing the pump laser wavelength, are almost identical to those in the ps-R2PI spectrum. This situation is somewhat different from previous ns results, where the ns-R2PI signal diminishes at around 1000 cm^{-1} above the S_1 origin, while the ns-PHOFEX signal starts to increase with a broad background at around the same internal energy.[31] The difference between ns-R2PI and ns-PHOFEX could now be firmly ascribed to a decrease of the excited-state lifetime with increasing the excitation energy, as reflected in the similarity between ps-R2PI and ps-PHOFEX spectra.

Now, state-specific excited-state lifetimes or fragment appearance rates are measured in real time for all spectrally resolved S_1 vibronic levels of thioanisole. A picosecond parent-ion transient taken at the S_1 zero-point level gives the single-exponential decay with $\tau \approx 2100 \pm 43$ ps, Figure 3, which is quite consistent with the previously reported S_1 lifetime of 2.0 ns from a high-resolution spectroscopic study of the same system.[39] The CH_3^+ fragment transient taken by detecting the whole CH_3 ($v = 0$) signal, on the other hand, shows a single-exponential rise to give an associated lifetime of ~2080 ± 130 ps. These parent-decay and fragment-rise time constants are identical within uncertainties, indicating that fragmentation is a direct consequence of the excited-state decay. It should be noted that there is a small but very fast component in the CH_3^+ transient that is due to fragmentation of the parent ion
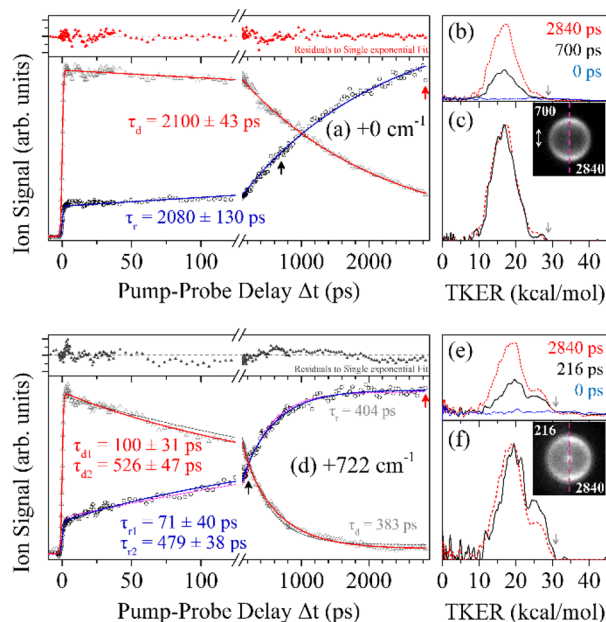

Figure 3. Ion yield transients and ps-resolved total kinetic energy release (TKER) distributions. (Left column) Time-resolved transients of $C_6H_5SCH_3^+$ (gray triangles) and CH_3^+ (black circles) along with kinetic fit analyses (solid lines) measured at (a) the S_1 origin and (d) +722 cm^{-1}. Transients at +722 cm^{-1} (d) show faster dynamics, and their fits with two time constants (solid lines) are much better compared to fits with a single time constant (dashed lines). Relative amplitude ratios of faster components are estimated to be 0.22 or 0.13 from biexponential fits to a $C_6H_5SCH_3^+$ or CH_3^+ transient, respectively. Residual analyses are given for the parent transients for single-exponential fits to the experiment in (a) and (d). Single-exponential fit to the experiment at 722 cm^{-1} gives consistent negative values for the (experiment − fit) difference, indicating that a biexponential fit including the fast component is necessary. (Right column) Three-point averaged TKER distributions deduced from CH_3^+ images excited at (b) the S_1 origin and (e) +722 cm^{-1} at different pump−probe time delays. Normalized distributions after subtraction of the time-zero distribution (blue dashed) are shown in (c) and (f). Vertical gray arrows indicate the maximum TKER value predicted with the dissociation energy value[37] of 24 400 cm^{-1}. Halves of symmetrized raw images before reconstruction at two different reaction times (unit in ps) are given in the insets of (c) and (f).

generated by multiphoton excitation at the zero delay time. This multiphoton effect has been properly taken into account in our fits to the experiment. With increasing the excitation energy, it is found that the overall predissociation rate, represented by time constants of both parent decay and fragment rise, increases very rapidly. For instance, it is surprising that the reaction rate is almost doubled as the internal energy is increased from the zero-point energy to only 69 cm^{-1} (see also the Supporting Information). The rate constant then remains more or less constant at the vibronic mode at 128 cm^{-1}, whereas it even slightly decreases at 202 cm^{-1}. This mode-dependent variation of reaction rate continues up to a vibronic band at 390 cm^{-1}, indicating that the reactive flux in this energy regime does not behave statistically. Although assignments for all S_1 vibronic levels had been properly carried out in our previous reports,[31] we do not try to explain the origin of mode-dependent rate constants at the present time. As the internal energy increases further, the reaction rate constant increases exponentially, Figure 2. The overall pattern of the reaction rate change with increasing the

internal energy is quite interesting, although multidimensional dynamics calculations seem to be required for a satisfactory explanation.

The most interesting and remarkable observation is that both parent and fragment transients taken at the S_1 internal energy of 722 cm^{-1} could not be described with a single-exponential function, whereas transients taken at all other S_1 vibronic modes are fitted very well with a single-exponential function. Rather, a biexponential function has to be employed for reproducing the experiment, giving two distinct lifetimes of 100 ± 31 (or 71 ± 40) and 526 ± 47 (or 479 ± 38) ps as fast and slow components, respectively, of the parent (or fragment) transient at 722 cm^{-1}. Generally, biexponential decay of the parent excited state had been often attributed to IVR in many other systems.[40−42] However, the experimental finding that both parent and fragment transients are biexponential in their temporal dynamics strongly indicates that the reactive flux prepared by 7a vibronic mode excitation undergoes predissociation along two distinct reaction pathways, of which reaction rates are 5 or 7 times different from each other. In order to clarify the biexponential behavior of the predissociation dynamics at 722 cm^{-1}, time-dependent product state distributions are precisely measured, as energy disposal into final fragments is expected to be quite different for two distinct predissociation channels with different reaction rates.

The total product translational energy distribution at the S_1 zero-point level of thioanisole is obtained from a series of VMI images of the $\cdot CH_3$ ($v = 0$) fragment taken as a function of pump−probe delay time, Figure 3. Obviously, there is no discernible fragment signal at the zero delay time. The shape of the translational energy distribution obtained at the middle of the reaction (Δt = 700 ps) is identical to that obtained in the asymptotic region (Δt = 2840 ps) except for their absolute total intensities. This experimental fact is consistent with single-exponential kinetics observed at the S_1 zero-point energy level, suggesting that fragmentation dynamics is the consequence of the single reaction path. The situation is however quite different for the translational distribution obtained at 722 cm^{-1}. As reported in our previous result in the frequency domain,[31] the high kinetic energy portion shown as a shoulder in the bimodal distribution corresponds to the nonadiabatic channel giving the $C_6H_5S\cdot(\tilde{X})$ fragment, whereas the adiabatic channel leading to $C_6H_5S\cdot(\tilde{A})$ is associated with the low kinetic energy portion. Notably, at this 7a mode excitation, the shape of the translational energy distribution obtained at an early reaction time of 216 ps turns out to be quite distinct from that measured at the asymptotic time delay of 2840 ps. At the early reaction time, the high kinetic energy portion stands out compared to that obtained at the asymptotic level. The average kinetic energy of fragments measured at 216 ps is a bit higher than that obtained at 2840 ps. Variation of dynamic outputs at different reaction times clearly indicates that there exist two different reaction pathways of which reaction rates are quite distinct. Apparently, judging from the difference between translational energy distributions on changing the reaction time, the high kinetic energy portion associated with the nonadiabatic channel seems to grow faster compared to the low kinetic energy portion, corresponding to the adiabatic channel, ascertaining the above-mentioned biexponential behavior of the 722 cm^{-1} transients (see the Supporting Information for more details).

This provides an invaluable clue for the explanation of nonadiabatic dynamic resonance at the 7a mode excitation. As the S_1/S_2 conical intersection region is supposed to be accessed by the 7a mode excitation, the excited-state wave function is strongly perturbed due to the breakdown of the Born−Oppenheimer approximation. Based on the concept that wave function in the conical intersection region is the result of the S_1/S_2 nonadiabatic state mixing, one may then not explicitly but simply depict the wave function of the 722 cm^{-1} mode (ψ) as a sum of adiabatic and diabatic functions as follows.

$$\psi = c_1\varphi_a + c_2\varphi_d \tag{1}$$

Here, φ_a and φ_d are eigenfunctions in adiabatic and diabatic potential energy surfaces in the vicinity of the conical intersection with coefficients of c_1 and c_2, respectively. Depending on the nonadiabatic coupling strength given along the 7a mode vibrational degree of freedom near the conical intersection, the corresponding wave function could be more like adiabatic or diabatic. Equation 1 could be rationalized, as it may not be appropriate to describe the wave function near the conical intersection with either an adiabatic or diabatic basis set only. In the curve-crossing region along the 7a mode, φ_d represents the eigenfunction on the diabatic $\pi\pi^*$ state (lower-bound), whereas φ_a resides on the adiabatic potential energy surface generated by avoided crossing of bound $\pi\pi^*$ and repulsive $n\sigma^*$ (S_2, upper-bound) mediated by vibronic coupling. As the nuclear momentum vector being enforced by the repulsive $n\sigma^*$ is not necessarily the same as that restored by the bound $\pi\pi^*$ in the upper-bound adiabat, φ_a may represent the projection of the upper-bound eigenfunction on the optically active 7a normal mode coordinate in terms of its spanning phase space. Further higher-order state-mixing between φ_d and φ_a is nontrivial to estimate, as perturbation is intrinsically multidimensional in nature. Now, decay of reactive flux, which may represent temporal dynamics of $|\psi|^2$ in the real part, can be expressed as follows.

$$\frac{d|\psi|^2}{dt} \propto c_1{}^2\frac{d|\varphi_a|^2}{dt} + c_2{}^2\frac{d|\varphi_d|^2}{dt} + \ldots \tag{2}$$

Even after neglecting the interference terms assuming that φ_a and φ_d are not coherently excited, the parent excited state will not follow single-exponential decay if $|\varphi_a|^2$ and $|\varphi_d|^2$ have different decay time constants. It should be noted here that this contrasts with elemental kinetics of one reactant state bifurcating into two different channels with distinct rate constants of k_1 and k_2, for example. In the latter case, both reactant decay and fragment rise are supposed to be single-exponential with the same time constant, corresponding to the inverse of the total rate constant of $k = k_1 + k_2$.

The reactive flux at the 722 cm^{-1} mode, from the moment of preparation, consists of two distinct components that decay with different rate constants of k_a and k_d for φ_a and φ_d states, respectively. Now, which one is faster than the other? For all other vibronic modes except 722 cm^{-1}, as $\pi\pi^*$ and $n\sigma^*$ apparently do not cross along corresponding normal mode coordinates, the wave function of the reactive flux is expected to be more like φ_d according to the above definition. Namely, the reactive flux initially bound in the diabatic $\pi\pi^*$ state explores restricted or the entire phase space before it is eventually coupled to the repulsive part of $n\sigma^*$. The reactive flux of φ_d in this case is then likely to take the adiabatic potential energy surface having a saddle point along the reaction coordinate,[43] as the probability for the upper-bound adiabat formation with respect to corresponding vibronic modes should be quite low. Consequently, k_d is expected to be small at least in the low

internal energy region, as it would take time for the reactive flux to find the trough of the potential energy surface along the reaction coordinate. With increasing the internal energy, k_d will increase as the search for the saddle point along the reaction path would be facilitated for the more flexible and expandable reactive flux prepared at the higher internal energy. This behavior is consistent with that of the slow component of the transient taken at 722 cm^{-1}, as corresponding lifetimes conform to the trend of lifetime over the entire energy range, giving k_d^{-1} = 526 ± 47 (or 479 ± 38) ps determined from the biexponential fit to the parent (or fragment) transient (Figure 2 and Table S1). This leads us to conclude that fast component of the parent (or fragment) transient at 722 cm^{-1} with k_a^{-1} = 100 ± 31 (or 71 ± 40) ps is responsible for the decay of the φ_a state. In the predissociation process, the φ_a state undergoes a nonadiabatic transition through CI-1 to ride on the repulsive $n\sigma^*$ state before it bifurcates into the adiabatic or nonadiabatic channel at CI-2 (Figure 1). The upper-bound adiabatic potential is supposed to be generated in the much reduced dimensionality, as the $n\sigma^*$ state is repulsive only along the S−CH$_3$ elongation coordinate. Therefore, evolution of the φ_a state within the upper adiabatic potential is quite limited in the nuclear configuration space. Furthermore, nuclear momentum enforced by the repulsive part in the upper adiabat will facilitate a nonadiabatic transition at the S$_1$/S$_2$ conical intersection. These two factors may be responsible for why the reaction rate of φ_a would be faster than that of φ_d. In other words, the reaction path of the φ_a flux is relatively restricted, so that it is driven efficiently to the reaction coordinate through the S$_1$/S$_2$ conical intersection. This makes the reaction rate of φ_a faster than that of φ_d, as the flux has to explore the larger phase space along many degrees of freedom to reach the saddle point of the adiabatic potential surface for the latter case.[43]

In order to further separate two distinct fragmentation dynamics in the temporal domain, we have obtained a series of VMI images at many different reaction times, Figure 4. The resulting two-dimensional spectrum taken along the reaction time and product translational energy is then globally analyzed using the following Gaussian-convoluted sum of exponential rise functions including the Heaviside step function.

$$I(\text{TKER}, \Delta t) = \int_{-\infty}^{\infty} e^{-\left(\frac{\Delta t - x}{w}\right)^2} \left[\text{heaviside}(x - t_0)\right.$$
$$\times \{c_1(\text{TKER})(1 - e^{-\left(\frac{x - t_0}{\tau_1}\right)})$$
$$\left. + c_2(\text{TKER})(1 - e^{-\left(\frac{x - t_0}{\tau_2}\right)})\}\right] dx \qquad (3)$$

A nonlinear least-square fit to the experiment then gives shapes of fast and slow components as well as their respective time constants and amplitudes. Our fit to the experiment at 722 cm^{-1} gives time constants of 84 and 524 ps for fast and slow components, respectively, which are quite consistent with those obtained from the whole fragment transient (Figure 3). It is remarkable that the translational energy distribution of the slow dynamic channel extracted from this analysis is almost identical to that of the whole channel observed for neighboring vibronic levels other than 722 cm^{-1}, giving the $\tilde{X}/\tilde{A}$ product branching ratio of ∼0.04 (see Supporting Information). This indicates that the φ_d flux tends to remain on the adiabatic path at CI-2 since it is expected to be vibrationally excited orthogonal to the reaction coordinate as it passes through the S$_1$ adiabatic saddle point located out of the molecular plane.[43] This seems to apply to dynamics occurring at all other vibronic modes in the 0−
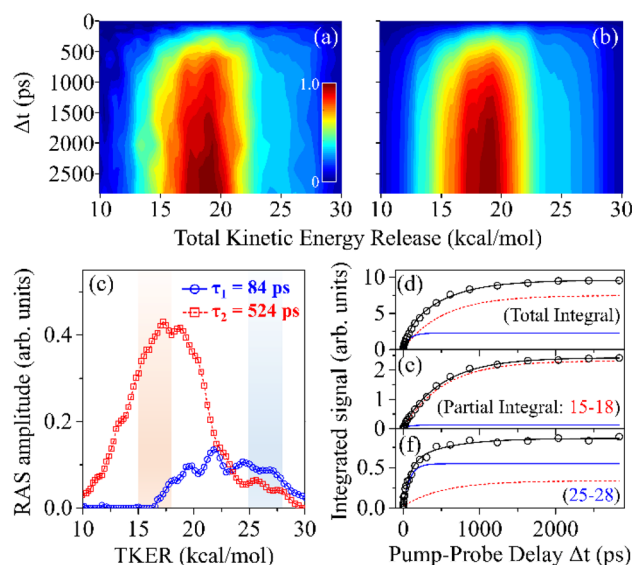

Figure 4. Time-resolved CH$_3^+$ ion imaging results following excitation at +722 cm^{-1} and its global analysis. (a) Two-dimensional map showing TR-VMI results with respect to TKER and reaction time. The VMI image taken at the zero delay time was subtracted in order to exclude the contribution from multiphoton excitation. (b) Global fit to the experiment modeled with two exponential rise functions (see Supporting Information for details). (c) Rise associated spectra (RAS) from the global fit, showing two rising components with τ_1 = 84 ps (blue circle) and τ_2 = 524 ps (red square). Transients of fragment signals distributed over (d) entire, (e) low, or (f) high TKER distribution are shown with fast (τ_1, blue solid) and slow (τ_2, red dashed) fits. TKER regions used for partial integrations are depicted with red (15−18 kcal/mol, e) and blue (25−28 kcal/mol, f) shades. While the fast component of τ_1 is negligible in (e), it stands out in the transient monitoring the fast component in (f).

2000 cm^{-1} region of the S$_1$ internal energy. The translational energy distribution of the fast component with τ = 84 ps, on the other hand, is much different from that of the slow component in terms of both its average kinetic energy and $\tilde{X}/\tilde{A}$ product branching ratio. The translational energy distribution of the adiabatic channel associated with C$_6$H$_5$S·($\tilde{A}$) from φ_a is largely shifted to the higher kinetic energy region compared to that from the φ_d flux. This means that final fragments are vibrationally less excited for the φ_a flux. More intriguingly, the $\tilde{X}/\tilde{A}$ product branching ratio of the fast component is substantially high, to give ∼0.9. This indicates that the nonadiabatic transition probability of φ_a at CI-2 is exceptionally high, reinforcing our interpretation that the φ_a flux funneled through the first S$_1$/S$_2$ conical intersection funnels through CI-2 more efficiently with high probability, as these two conical intersections are connected by repulsive $n\sigma^*$. The relatively less vibrational excitation of fragments is also anticipated for the φ_a flux especially because vibrational energy in the upper-bound adiabat is likely to be transformed into kinetic energy due to the repulsive nature of the upper adiabat along the reaction coordinate. Time-resolved fragmentation dynamics now explain our previous observation obtained in the frequency domain quite well. Namely, resonance-like increases of the $\tilde{X}/\tilde{A}$ product branching ratio (∼0.4) and the translational energy partitioning ratio[31] are actually due to concomitant excitation of the metastable quantum state (φ_a) confined in the upper-bound adiabat near the conical intersection.

CONCLUSIONS

Here, we located the conical intersection in the nuclear configurational space and then investigated the associated nonadiabatic dynamics in real time for the title system. This is the first example where both spatial and temporal characterization of the conical intersection could be accomplished simultaneously for a polyatomic molecule. When the reactive flux is prepared in close proximity to the conical intersection in the predissociation of thioanisole, two distinct adiabatic and nonadiabatic reaction pathways are found to coexist. Reaction rates of these channels, as well as dynamic outputs such as product branching ratios and product state distributions, are found to be quite different from each other. Our time-resolved measurement of the product state distribution could separate the two distinct dynamic channels unambiguously, unraveling the detailed mechanism of nonadiabatic dynamics occurring in the vicinity of the conical intersection. The nonadiabatic channel resulting from the reactive flux passage through two consecutive conical intersections as dynamic funnels is found to be faster than the adiabatic channel, where the reactive flux explores the phase space looking for the trough of the potential energy surface along the reaction coordinate. Specifically, the 722 cm^{-1} (7a) mode excitation activates the new efficient and faster nonadiabatic reaction channel that has been realized by surface-crossing of S_1 ($\pi\pi^*$) and S_2 ($n\sigma^*$) along the corresponding nuclear coordinate. As our experiment here has revealed a detailed nonadiabatic dynamic mechanism taking place in the proximity of the conical intersection for the first time, high-level calculations of multidimensional potential energy surfaces would be quite timely and highly desirable for a thorough understanding of whole nonadiabatic dynamics. Interferences caused by "resonances in continuum" especially generated by surface crossings[44] are of keen interest to be searched. Incidentally, distinct temporal dynamics of nonadiabatic and adiabatic channels found here suggest a new way of nonadiabatic reaction control. Namely, one can employ the pump−perturb−probe laser excitation scheme. Here, pump prepares the reactant flux near the conical intersection, while perturb depopulates the excited state and probe monitors the final products. By changing the delay time between pump and perturb laser pulses, for instance, one may be able to control the relative ratio of the fast and slow reaction channels. This will lead to the control of nonadiabaticity of chemical reactions.

EXPERIMENTAL METHODS

Picosecond pump−probe laser pulses were generated starting from the 1 kHz synchronized fs/ps Ti:sapphire regenerative amplifier system seeded with a fs oscillator (Legend Elite-USP/P, Vitara-T-HP, Coherent). Tunable ultraviolet frequencies for pump/probe wavelengths were obtained by nonlinear mixing of pulses from two optical parametric amplifiers (TOPAS-800 ps, Light Conversion) pumped by the 50:50 split fundamental outputs. The time-resolved experimental pump−probe scheme is depicted in Figure 1. Pump (λ_1 = 291−271 nm) was used for the initial population of the $\pi\pi^*$ state, whereas probe laser pulses were used to detect $C_6H_5SCH_3^+$ (λ_2 = 300 nm) or CH_3^+ (λ_2 = 333.5 nm for the (2 + 1) resonance ionization of CH_3 (v = 0) via $3p_z$). Two pulses were nearly collinearly aligned and focused on the gas mixture in the pulsed supersonic jet with planoconvex spherical lenses (f = 300 mm). The entrance window of the chamber was 1 mm thick. Temporal delays between pump and probe pulses (Δt) were scanned from −20 ps to the temporal limit of 2.84 ns by employing a double-pass alignment scheme using a broadband hollow retroreflector (UBBR2.5-1UV, Newport) mounted on a computer-controlled 220 mm optical delay line (DDS220, Thorlabs). Thioanisole (Sigma-

Aldrich) was heated to 80 °C, bubbled with 2 bar of neon carrier gas, and expanded into a vacuum through a nozzle orifice operated by a 20 Hz pulsed valve (General Valve series 9, Parker) before it was skimmed through a 1 mm diameter skimmer (Beam Dynamics). The imaging spectrometer consists of two differentially pumped vacuum chambers. Source and ionization chambers were evacuated with two turbomolecular pumps with pumping rates of 2300 and 800 L/s (HiPace 2300/800, Pfeiffer Vacuum), respectively, while each foreline was pumped by a dry pump (ACP 40G/28G, Alcatel). The conventional VMI electrodes[45] accelerate ions through a 30-cm-long time-of-flight region to the two-dimensional position-sensitive detector (PSD) equipped with Chevron-type microchannel plates (MCPs) backed by a P46 phosphor (Photonis). For VMI measurements, a pulsed voltage gate was applied to the MCPs with a high voltage pulse generator (PVX-4140, DEI) to select a specific mass-to-ratio of ions. The images on the phosphor screen were captured by a CCD camera (UI-2230SE-M-GL, IDS). Each image obtained at a specific time delay was three-dimensionally reconstructed with the polar onion peeling method.[46] The measured kinetic energy distributions were calibrated with the one-color (2 + 1) resonance-enhanced ionization of xenon at 250 nm. Polarizations of both laser beams were parallel with the PSD. When parent ion transients were taken, a $\lambda/2$ waveplate was employed to rotate the polarization axis of the probe laser pulse so that the polarization angle between the pump and probe is 54.7° (magic angle) in order to rule out any rotational dephasing effect.

ASSOCIATED CONTENT

Ⓢ Supporting Information

The Supporting Information is available free of charge on the ACS Publications website at DOI: 10.1021/jacs.7b09677.

> Ion yield transients measured at all vibronic levels, details of fitting procedures, product state distributions at representative time delays for different vibronic bands, deconvolution procedure for the rise associated spectra, and analyses of TR-VMI with a single time constant (PDF)

AUTHOR INFORMATION

Corresponding Author
*sangkyukim@kaist.ac.kr

ORCID Ⓞ
Kyung Chul Woo: 0000-0002-9387-9397
Sang Kyu Kim: 0000-0003-4803-1327

Notes
The authors declare no competing financial interest.

ACKNOWLEDGMENTS

REFERENCES

(1) Herzberg, G. *Electronic Spectra and Electronic Structure of Polyatomic Molecules*; Van Nostrand, 1966.
(2) Schinke, R. *Photodissociation Dynamics: Spectroscopy and Fragmentation of Small Polyatomic Molecules*; Cambridge University Press, 1995.
(3) Dobbyn, A.; Mordaunt, D.; Schinke, R. In *Springer Handbook of Atomic, Molecular, and Optical Physics*; Drake, G., Ed.; Springer: New York, 2006; p 535.
(4) Heumann, B.; Weide, K.; Düren, R.; Schinke, R. *J. Chem. Phys.* **1993**, *98*, 5508.
(5) Balerdi, G.; Woodhouse, J.; Zanchet, A.; de Nalda, R.; Senent, M. L.; Garcia-Vela, A.; Banares, L. *Phys. Chem. Chem. Phys.* **2016**, *18*, 110.

(6) Nadler, I.; Noble, M.; Reisler, H.; Wittig, C. *J. Chem. Phys.* **1985**, *82*, 2608.

(7) Hennig, S.; Engel, V.; Schinke, R.; Nonella, M.; Huber, J. R. *J. Chem. Phys.* **1987**, *87*, 3522.

(8) Hennig, S.; Untch, A.; Schinke, R.; Nonella, M.; Huber, J. R. *Chem. Phys.* **1989**, *129*, 93.

(9) Rosker, M. J.; Rose, T. S.; Zewail, A. H. *Chem. Phys. Lett.* **1988**, *146*, 175.

(10) Beswick, J. A. In *Dynamical Processes in Molecular Physics*; Delgado-Barrio, G. Ed.; IOP Publishing: Bristol, 1993; p 183.

(11) Kato, H.; Baba, M. *Chem. Rev.* **1995**, *95*, 2311.

(12) Worth, G. A.; Cederbaum, L. S. *Annu. Rev. Phys. Chem.* **2004**, *55*, 127.

(13) Domcke, W.; Yarkony, D. R. *Annu. Rev. Phys. Chem.* **2012**, *63*, 325.

(14) Han, S.; Lim, J. S.; Yoon, J. H.; Lee, J.; Kim, S. Y.; Kim, S. K. *J. Chem. Phys.* **2014**, *140*, 054307.

(15) You, H. S.; Han, S.; Lim, J. S.; Kim, S. K. *J. Phys. Chem. Lett.* **2015**, *6*, 3202.

(16) Mozhayskiy, V. A.; Babikov, D.; Krylov, A. I. *J. Chem. Phys.* **2006**, *124*, 224309.

(17) You, H. S.; Han, S.; Yoon, J. H.; Lim, J. S.; Lee, J.; Kim, S. Y.; Ahn, D. S.; Lim, J. S.; Kim, S. K. *Int. Rev. Phys. Chem.* **2015**, *34*, 429.

(18) Horio, T.; Fuji, T.; Suzuki, Y.; Suzuki, T. *J. Am. Chem. Soc.* **2009**, *131*, 10392.

(19) Polli, D.; Altoe, P.; Weingart, O.; Spillane, K. M.; Manzoni, C.; Brida, D.; Tomasello, G.; Orlandi, G.; Kukura, P.; Mathies, R. A.; Garavelli, M.; Cerullo, G. *Nature* **2010**, *467*, 440.

(20) Worner, H. J.; Bertrand, J. B.; Fabre, B.; Higuet, J.; Ruf, H.; Dubrouil, A.; Patchkovskii, S.; Spanner, M.; Mairesse, Y.; Blanchet, V.; Mevel, E.; Constant, E.; Corkum, P. B.; Villeneuve, D. M. *Science* **2011**, *334*, 208.

(21) Musser, A. J.; Liebel, M.; Schnedermann, C.; Wende, T.; Kehoe, T. B.; Rao, A.; Kukura, P. *Nat. Phys.* **2015**, *11*, 352.

(22) Yoon, J. H.; Woo, K. C.; Kim, S. K. *Phys. Chem. Chem. Phys.* **2014**, *16*, 8949.

(23) Ahn, D. S.; Lee, J.; Choi, J. M.; Lee, K. S.; Baek, S. J.; Lee, K.; Baeck, K. K.; Kim, S. K. *J. Chem. Phys.* **2008**, *128*, 224305.

(24) Epshtein, M.; Yifrach, Y.; Portnov, A.; Bar, I. *J. Phys. Chem. Lett.* **2016**, *7*, 1717.

(25) Sage, A. G.; Nix, M. G. D.; Ashfold, M. N. R. *Chem. Phys.* **2008**, *347*, 300.

(26) Rodrigo, C. P.; Zhou, C.; Reisler, H. *J. Phys. Chem. A* **2013**, *117*, 12049.

(27) Matsika, S.; Krause, P. *Annu. Rev. Phys. Chem.* **2011**, *62*, 621.

(28) Malhado, J. P.; Bearpark, M. J.; Hynes, J. T. *Front. Chem.* **2014**, *2*, 97.

(29) Yang, K. R.; Xu, X. F.; Zheng, J. J.; Truhlar, D. G. *Chem. Sci.* **2014**, *5*, 4661.

(30) Curchod, B. F.; Rauer, C.; Marquetand, P.; Gonzalez, L.; Martinez, T. J. *J. Chem. Phys.* **2016**, *144*, 101102.

(31) Lim, J. S.; Kim, S. K. *Nat. Chem.* **2010**, *2*, 627.

(32) Kim, J. B.; Yacovitch, T. I.; Hock, C.; Neumark, D. M. *Phys. Chem. Chem. Phys.* **2011**, *13*, 17378.

(33) Lee, J.; Kim, S. Y.; Kim, S. K. *J. Phys. Chem. A* **2014**, *118*, 1850.

(34) Kim, S. Y.; Lee, J.; Kim, S. K. *Phys. Chem. Chem. Phys.* **2017**, *19*, 18902.

(35) Roberts, G. M.; Williams, C. A.; Young, J. D.; Ullrich, S.; Paterson, M. J.; Stavros, V. G. *J. Am. Chem. Soc.* **2012**, *134*, 12578.

(36) Roberts, G. M.; Chatterley, A. S.; Young, J. D.; Stavros, V. G. *J. Phys. Chem. Lett.* **2012**, *3*, 348.

(37) Roberts, G. M.; Hadden, D. J.; Bergendahl, L. T.; Wenge, A. M.; Harris, S. J.; Karsili, T. N. V.; Ashfold, M. N. R.; Paterson, M. J.; Stavros, V. G. *Chem. Sci.* **2013**, *4*, 993.

(38) Roberts, G. M.; Williams, C. A.; Yu, H.; Chatterley, A. S.; Young, J. D.; Ullrich, S.; Stavros, V. G. *Faraday Discuss.* **2013**, *163*, 95.

(39) Hoshino-Nagasaka, M.; Suzuki, T.; Ichimura, T.; Kasahara, S.; Baba, M.; Kawauchi, S. *Phys. Chem. Chem. Phys.* **2010**, *12*, 13243.

(40) Perry, J. W.; Scherer, N. F.; Zewail, A. H. *Chem. Phys. Lett.* **1983**, *103*, 1.

(41) Smith, J. M.; Zhang, X.; Knee, J. L. *J. Phys. Chem.* **1995**, *99*, 1768.

(42) Kosma, K.; Schröter, C.; Samoylova, E.; Hertel, I. V.; Schultz, T. *J. Am. Chem. Soc.* **2009**, *131*, 16939.

(43) Li, S. L.; Truhlar, D. G. *J. Chem. Phys.* **2017**, *146*, 064301.

(44) Cederbaum, L. S.; Friedman, R. S.; Ryaboy, V. M.; Moiseyev, N. *Phys. Rev. Lett.* **2003**, *90*, 013001.

(45) Eppink, A. T. J. B.; Parker, D. H. *Rev. Sci. Instrum.* **1997**, *68*, 3477.

(46) Roberts, G. M.; Nixon, J. L.; Lecointre, J.; Wrede, E.; Verlet, J. R. *Rev. Sci. Instrum.* **2009**, *80*, 053104.